*Pramana – J. Phys.* (2019) 93:85
https://doi.org/10.1007/s12043-019-1849-5


# Commissioning and validation of the injector and electron beam transport systems for the IR-FEL at RRCAT

SONA CHANDRAN[1,*], BHASKAR BISWAS[1], SHANKAR LAL[1], ARVIND KUMAR[1], R S SAINI[1], M KHURSHEED[2], SAKET KUMAR GUPTA[1], PRAVIN NERPAGAR[1], R K PANDIT[1] and K K PANT[1]

[1]Free Electron Laser and Utilization Section, Raja Ramanna Centre for Advanced Technology, Indore 452 013, India
[2]Advanced Lasers and Optics Division, Raja Ramanna Centre for Advanced Technology, Indore 452 013, India
*Corresponding author. E-mail: sona@rrcat.gov.in

MS received 16 July 2018; revised 6 April 2019; accepted 27 June 2019

**Abstract.** The first observation of lasing in an infra-red free electron laser (IR-FEL) at the Raja Ramanna Centre for Advanced Technology has been reported recently with a measured power output, i.e. $\sim 10^5$ times higher than the expected spontaneous radiation power for the electron beam parameters used in the experiment. IR-FEL design simulations, however, estimate a power gain of $10^7$ which is three orders of magnitude higher than the experimentally achieved value. To understand this difference between the measured and the expected power output from the IR-FEL, the electron beam used in the experiments has been characterised and FEL simulations have been repeated after considering the measured electron beam parameters. A reasonably good agreement is obtained between the measured results and those predicted by FEL simulations. Experiments have also been performed to study the expected variation in electron beam properties over a macropulse, which should be minimum for an oscillator FEL like the IR-FEL. This paper reports the results from the experiments for characterisation of the electron beam in the IR-FEL set-up and the results from FEL simulations, considering these measured electron beam parameters.

**Keywords.** Free electron laser; beam parameters; infra-red power.

**PACS Nos 41.60.Cr; 29.27.–a; 07.57.Hm**

## 1. Introduction

An infra-red free electron laser (IR-FEL) operating in the 12.5–50 $\mu$m wavelength range is in an advanced stage of commissioning at the Raja Ramanna Centre for Advanced Technology (RRCAT), Indore, India [1–3]. The important design parameters of the IR-FEL are given in table 1.

The IR-FEL set-up employs an injector system with an indigenously developed subharmonic pre-buncher (SHPB) followed by two indigenously developed plane-wave transformer (PWT)-type standing wave linear accelerator (linac) structures to deliver an electron beam of ~18.4 MeV energy and ~25 A peak current. This electron beam is transported to the optical cavity region by employing an isochronous and achromatic electron beam transport line, which is also used to select a fraction of the charge with the required relative energy spread, and to manipulate the transverse electron beam parameters to that required at the entry to the undulator. Inside the IR-FEL optical cavity, the electron beam is propagated through its undulator, which is a pure permanent magnet (PPM)-type undulator with 5 cm period, variable undulator parameter (0.5–1.2) and with a total length of 2.5 m. More details of the IR-FEL set-up are given in ref. [2], and a schematic of the IR-FEL set-up is shown in figure 1.

As lasing in an FEL involves a resonant interaction between a relativistic electron beam and a co-propagating electromagnetic wave in the presence of an undulator, successful operation of the device critically depends upon the quality of the electron beam and the undulator magnetic field. The undulator magnetic field is static in time, and is produced by a periodic arrangement of PPMs. This field is mapped offline to ensure that the field quality is as per design, before it is installed in the FEL set-up. The accelerated electron beam quality, on the other hand, critically depends upon the quality and stability of the electron beam generated by the electron gun and on its subsequent acceleration by the

Published online: 04 October 2019

radio frequency (RF) accelerating structures employed in the injector linac system. Therefore, the quality of the RF and microwaves powering the different accelerating structures critically affects the quality and stability of the electron beam produced by the injector linac system. The important parameters that qualify an electron beam for an FEL are: (i) mean energy, which determines the central wavelength of radiation generated; (ii) relative energy spread, which affects the FEL interaction in the device; (iii) jitter in mean energy, which affects the gain critically because the central wavelength is different at different mean energies and (iv) emittance, which affects the overlap between the electron beam and the optical radiation as they propagate through the undulator. In addition to the aforementioned critical parameters, an additional parameter is introduced in an FEL operating in an oscillator configuration, as in the case of the IR-FEL. Due to the repeated interaction of an optical pulse reflecting back and forth inside the optical cavity of the FEL with subsequent electron bunches coming from the injector system, the jitter in arrival time of the electron microbunches at the undulator entry is required to be minimal to ensure good overlap between the electron and optical pulses over each pass. This timing jitter depends upon the stability of RF and microwaves powering the RF accelerating structures, and is a critical parameter for oscillator FELs.

**Table 1.** IR-FEL design parameters.

| | |
|---|---|
| Design wavelength | 12.5–50 $\mu$m |
| Design beam energy | 15–25 MeV |
| Small signal gain | ∼50% |
| Mean energy jitter | <0.2% |
| Undulator period/length | 5 cm/2.5 m |
| Repetition rate | 1–10 Hz |
| Average power | 15–30 mW @ 10 Hz |
| Peak power | ∼1.7 MW |

Recently, the first observation of lasing in the IR-FEL set-up has been reported with a measured power output that is estimated to be $\sim 10^5$ times higher than the expected spontaneous power output for the electron beam parameters employed in the experiment [1]. Although FEL simulations for the designed injector system predict a power gain that is approximately two orders of magnitude higher than the experimentally observed value, further experiments with improved electron beam transmission did not result in any enhancement in the power output from the set-up. Initial characterisation of the electron beam revealed that the peak current per micropulse was ∼26 A with a relative energy spread (<0.75%) compared to the current considered in design simulations (30 A) with 0.5% root mean square (RMS) energy spread. The uniformity of peak current with 0.75% relative energy spread over a train of micropulses in each macropulse of the accelerated electron beam was also poor. In subsequent experiments, the amplitude of the peak current could be improved to >30 A with a relative energy spread of 0.75%, through tuning of the injector system and the electron beam transport line. However, no improvement in FEL power gain is observed as the uniformity of the energy selected electron beam over a macropulse could not be improved. In order to study the variation between the measured and the expected power output as predicted by simulations, the electron beam employed in the experiments was characterised by measuring its energy spread, emittance and the uniformity of micropulses over a macropulse. IR-FEL simulations were subsequently repeated by considering the measured electron beam parameters, and a reasonably good agreement was obtained between the measured and the expected power output in this case. This paper discusses the results obtained from the initial experiments for the validation of the injector and electron beam transport systems of the IR-FEL.

In the next section, we briefly present the configuration of the IR-FEL injector system, and the scheme employed to achieve the desired electron beam

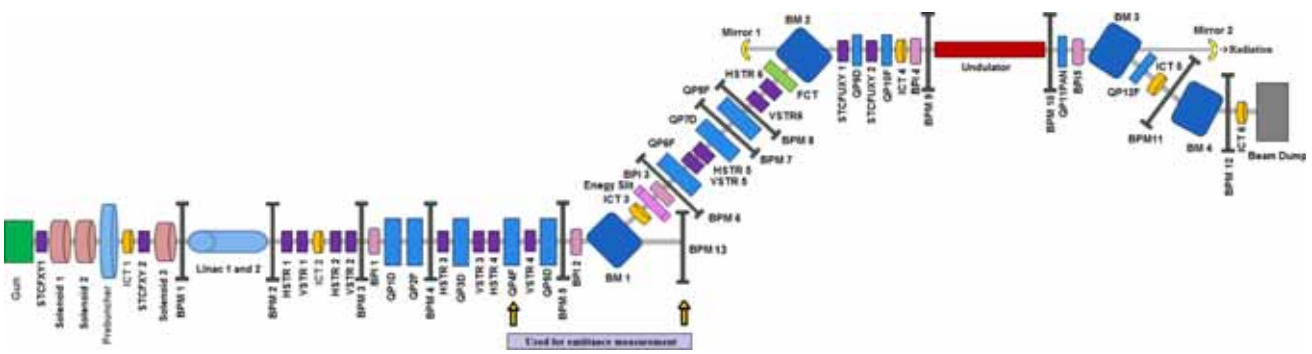


**Figure 1.** Lay-out of the IR-FEL system.

parameters. This is followed by a discussion of the commissioning of the IR-FEL injector system and validation of electron beam properties in §3. A discussion of the commissioning and validation of the electron beam transport line are given in §4 and the electron beam characterisation is discussed in §5. The results predicted by IR-FEL simulations after considering these measured electron beam parameters are given in §6. A summary of the work is presented in §7.

## 2. IR-FEL injector system configuration

Figure 2 shows a lay-out of the IR-FEL injector system. It is designed to deliver a train of 15–25 MeV electron bunches of 10 ps FWHM (full-width at half-maximum) with a peak electron beam current >30 A within the desired relative energy spread <0.5% and a normalised root mean square (RMS) emittance <30 mm mrad. The important subsystems of the IR-FEL injector system and the design input and output beam parameters at each subsystem are given below:

*Pulsed thermionic electron gun*: The source of electrons for the IR-FEL injector system is a 90 keV, pulsed thermionic electron gun capable of delivering 1 nC charge in 1 ns FWHM pulses at a repetition rate of 29.75 MHz (96th subharmonic of the main linac frequency of 2856 MHz) for a macropulse duration variable from 1 to 10 $\mu$s. The output electron bunches from the electron gun have an RMS radius of ∼4 mm at the waist and normalised RMS emittance <10 mm mrad.

*Subharmonic pre-buncher* (*SHPB*): The SHPB operating at 476 MHz (sixth subharmonic of the linac frequency of 2856 MHz) imparts a correlated velocity modulation of ∼30 keV to electrons in the 1 ns FWHM bunches coming from the thermionic electron gun, resulting in their bunching to ∼50–80 ps after a pre-determined drift space. The entry to the linac structures is located at this point.

*Plane-wave transformer* (*PWT*) *linac structures*: The IR-FEL set-up employs two cascaded 12-cell PWT linac structures, each capable of accelerating an electron bunch to ∼10 MeV energy consuming ∼4.5 MW peak RF power per structure. The total energy gain from the two PWT linac structures can be varied by varying the input microwave power fed to these structures. Initial commissioning trials were performed with a beam energy of ∼18.4 MeV. The PWT linac structures are $\beta = v/c \sim 1$ structures designed to accelerate a relativistic electron beam with ∼10 ps bunch length with minimum loss. However, in the initial commissioning trials of the IR-FEL injector system, a non-relativistic (90 keV) electron bunch of ∼50–80 ps bunch length was injected directly into the first PWT linac structure, where the first few cells acted as a buncher where the mean energy of a fraction of the 50–80 ps electron bunch injected into it was increased to a few MeV and the bunch length of this fraction was compressed to ∼10 ps. For subsequent cells of the first PWT linac structure, this beam has the desired input properties and it was accelerated further to design energy with minimum loss. More details of the IR-FEL injector linac system and the electron beam parameters at different stages of the injector system are presented in [4].

*Electron beam transport line*: The low-energy beam transport (LEBT) line consists of three thin solenoidal lenses and steering magnets to maintain the transverse size of the electron beam, and to correct beam trajectory along the injector system. It also has the provision for monitoring different electron beam parameters. After exiting the second PWT linac structure, the accelerated electron beam is transported further to the optical cavity region using the high-energy beam transport (HEBT) line, as discussed in subsequent sections. The HEBT is used to transport and manipulate the electron beam to deliver the desired transverse profile at the undulator entry. It also has provision for selecting a fraction of charge with the desired mean energy and relative energy spread, and for electron beam diagnostics. More details about the design of the HEBT are given in [5].

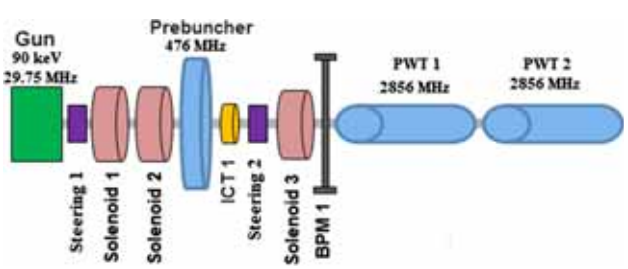


**Figure 2.** Lay-out of the IR-FEL injector system.

As discussed in the previous section, lasing in a FEL critically depends upon the quality of the electron beam delivered by its injector system, and on its overlap with the optical radiation inside its optical cavity. Therefore, validation of electron beam parameters through electron beam diagnostics during commissioning trials and a study of the agreement of results from IR-FEL simulations considering measured electron beam parameters with the measured optical radiation power is important for the successful commissioning of an

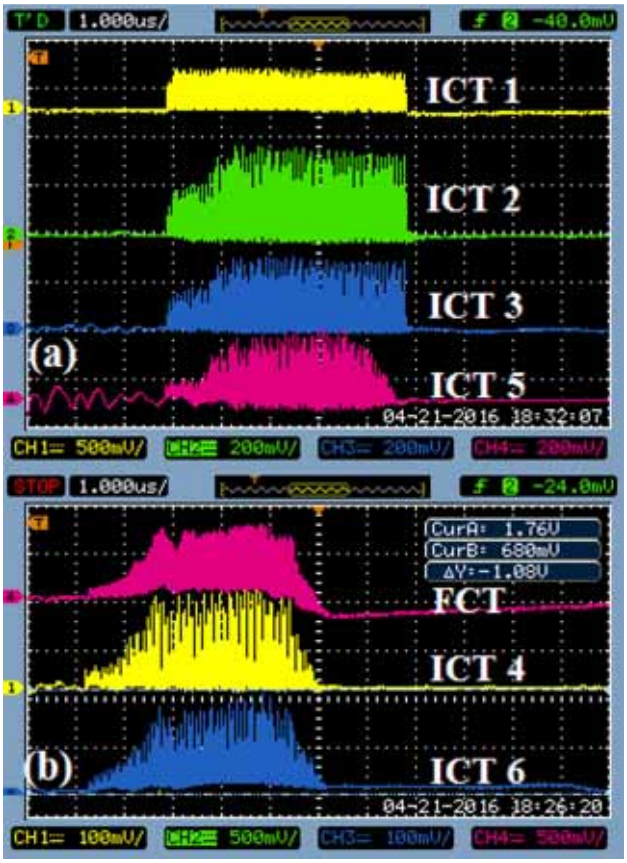


**Figure 3.** ICT traces of the electron beam at different locations in the IR-FEL. (**a**) ICT1 – after electron gun and before SHPB, ICT2 – exit of the linac, ICT3 – just after the first bending magnet before energy selection slit and ICT5 – at the undulator exit. (**b**) FCT before the second bending magnet, ICT4 – undulator entrance (after energy selection with RMS energy spread of <0.75%) and ICT6 – at the beam dump.

FEL. This is discussed in the subsequent sections of this paper.

## 3. IR-FEL injector system commissioning and validation

Commissioning of the IR-FEL injector system started with the generation and transport of a short pulse (1 $\mu$s), low charge electron bunch at 90 keV and its transport up to the entry of the first PWT linac structure. The charge in each micropulse from the electron gun was measured using an integrating current transformer (ICT) (Bergoz, ICT-122-015-5.0) while electron beam spot size is obtained using a beam profile monitor (BPM) with chromax screen and an image acquisition and analysis system developed in-house. Figures 3a and 3b show the macropulse structure of the electron beam at different positions along the IR-FEL set-up. The charge per micropulse is determined from the ICT traces by measuring the area under the curve on a digital storage oscilloscope (DSO) at 50 Ω impedance.

Since the time constant of the ICT is ∼5 ns, it cannot measure the precise time structure of each micropulse (∼1 ns) from the electron gun. However, the spacing between subsequent electron pulses is resolved truly by the ICT and a 500 MHz DSO (Lecroy Wave Runner LT-374). The charge per micropulse from the electron gun can be varied from 0.2 to 1 nC by varying its heater current while the macropulse width can be varied from 1 to 10 $\mu$s by varying the pulse width of the trigger signal to the electron gun. As reported in refs [4,6,7], an SHPB at 476 MHz bunches the 1 ns FWHM bunches from the electron gun to ∼50 ps at the entry of the first PWT linac. A loop-based RF power coupler feeds ∼2 kW RF power to set up the desired field gradient in the RF cavity with a re-entrant geometry [8]. With proper adjustment of the phase of the RF seen by each electron bunch as it enters the SHPB, a velocity modulation is introduced in the electrons in each bunch by the RF field, which results in the bunching of each microbunch after a drift distance that depends on the magnitude of velocity modulation introduced by the RF. For a 1 MV/m field gradient in the SHPB, each 1 ns bunch is compressed to ∼50 ps at the entry to the first PWT linac structure [4]. As this longitudinal compression can cause a transverse increase of bunch size due to space charge effects, a low-energy electron beam transport (LEBT) line has been built with low spherical aberration solenoids and steering magnets to guide the 90 keV electron bunches through the pre-buncher and into the linac [3,9]. The low spherical aberration helps to maintain a small beam size in the linac. Two 12-cell PWT linac structures are used in the IR-FEL injector system to obtain an energy gain of 18.4 MeV, consuming a total of ∼8.5 MW peak RF power in the two structures [10]. As the two PWT linac structures have slightly different RF properties, they are tuned to the desired resonant frequency of 2856 MHz by employing two independent precision chillers (Julabo Make-FC1600T). Before beginning beam trials using the PWT linac structures, the two structures were RF conditioned with progressively increasing pulse width, peak RF-power and repetition rate. In initial stages, starting with a base vacuum ∼1 × $10^{-8}$ mbar in both the structures, a steep deterioration of vacuum up to $10^{-6}$ mbar was observed during RF conditioning, which is improved rapidly with progressive RF conditioning of the structure till a stable base vacuum of ∼2 × $10^{-9}$ mbar and operating vacuum of ∼1–2 × $10^{-8}$ mbar are routinely achieved at rated power levels with macropulse width >5 $\mu$s and repetition rate up to 3 Hz. While the RF linac structures are qualified through low-level RF testing using a vector

**Table 2.** Comparison of RF properties of PWT1 and PWT2 measured during low-level RF power and high-power RF testing.

| Parameters | PWT1 | | PWT2 | |
|---|---|---|---|---|
| | Low-level RF test | High-power RF test | Low-level RF test | High-power RF test |
| Frequency, $f$ (MHz) | 2856.08 | 2856 at 30°C | 2856.08 | 2856 at 36°C |
| Quality factor (unloaded), $Q$ | 13248 | 17327 | 13377 | 16734 |
| Coupling coefficient, $\beta_{RF}$ | 1.03 | 1.41 | 1.22 | 1.52 |
| Shunt impedance, $R_{sh}$ (MΩ/m) | 51.53 | 67.39 | 45.43 | 52 |

network analyser (VNA) before their installation in the IR-FEL set-up, their properties at the rated high operation power level are often different from the low-power measurements. RF characterisation of the two 12-cell PWT linac structures in the IR-FEL injector system was done at rated power levels using traces of reflected power from the structures [11,12]. A comparison of RF properties of both the linac structures measured during the low-power RF testing and the parameters obtained from high-power tests is given in table 2 [12]. The improvement in quality factor (and thus in shunt impedance) of the PWT linac structures during high-power tests compared to the measured parameters during low-power tests is not fully understood, and is a subject of further investigation. This has been observed repeatedly in the different PWT linac structures developed by us, in addition to the two PWT linac structures employed in the IR-FEL set-up. This may be due to an improvement in the RF/electrical continuity of the central disk array with the end plate at high powers. By virtue of the geometry of the structure, there might be very minute gaps due to which RF contact may not be ideal at low electric fields. However, at high powers, the RF current jumps across the minute gaps and the improved RF contact results in higher measured $Q$ values, and consequently higher shunt impedance.

From the measured RF properties of the two PWT linac structures at rated power levels, the expected energy gain in the two structures was determined for different input RF powers as shown in figure 4. The high-power microwave line for powering the two PWT linac structures employs a 3 dB splitter to equally divide power from the klystron into two arms of the high-power microwave line. While the first arm goes directly to the PWT1 structure through a dual direction coupler (DDC) for sampling the forward and reflected power level in this arm, the second arm is connected to PWT2 through a high-power phase shifter and another DDC.

The high-power phase shifter is essential to fine tune the phase between high-power RF in the two linac structures to obtain sustained acceleration of the electrons in both the structures. The additional components of the high-power microwave line result in the arm feeding PWT2 to have a greater attenuation compared to the arm feeding PWT1. For 4.5 MW peak power fed to PWT1, PWT2 is fed ∼4 MW which leads to slightly different energy gains from both the structures. From figure 4, this translates to a maximum expected energy gain of ∼18.23 MeV after considering optimum settings of the high-power phase shifter in the PWT2 arm of the high-power microwave line. This is in good agreement with the measured beam energy of 18.4 MeV for the measured powers at the input ports of the two PWT linac structures, as discussed earlier. The measured energy gain translates to an average accelerating electric field gradient of ∼19.5 MV/m in the two structures by considering a total RF length of 1.26 m and a transit time factor of 0.75. The PWT1 structure, however, supports a higher gradient of ∼20 MV/m and PWT2 supports ∼19 MV/m. As discussed in [4], the accelerated electron beam at the exit of the injector system is expected to have a large relative energy spread of ∼22% because non-relativistic (90 keV) electrons with a large pulse width (∼50 ps) are injected into the S-band PWT linac structure, which is designed to accelerate a relativistic electron beam with $\beta \sim 1$. The maximum measured beam transmission through the linac structures was ∼54%, while ∼71% is predicted by simulations [4]. Selection of the fraction of charge with the desired relative energy spread (<0.5%) from the total accelerated charge is done using an energy selection slit installed in beam transport line of the first bend.

## 4. IR-FEL electron beam transport line commissioning and validation

The IR-FEL electron beam transport line is designed to transport and manipulate a round beam at the exit of the injector linac system to the required flat beam at the undulator entry, and to select the fraction of charge within each bunch having the desired relative energy spread [3,5]. Initial experiments on the transport of an accelerated electron beam through the IR-FEL set-up started with a short macropulse of 1 $\mu$s width with a low charge per microbunch (∼0.2 nC) from the electron gun. The transport line magnet settings were optimised to transport and manipulate the round beam at the linac exit

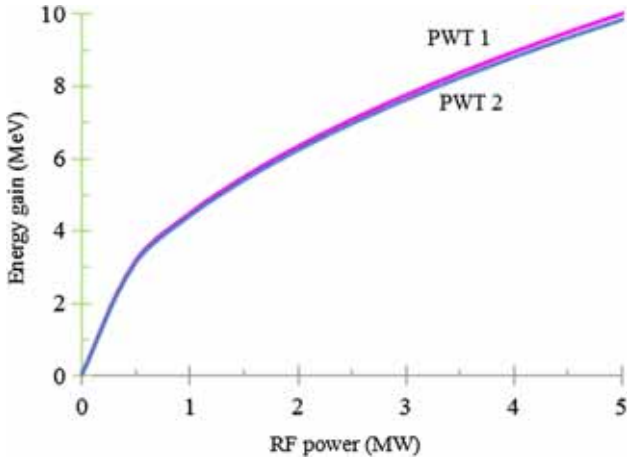


**Figure 4.** Expected energy gain in PWT1 and PWT2 linac structures with input RF power.

to a vertical beam with large dispersion near the energy selection slit and finally to a flat beam at the undulator entry. Figure 5 shows the beam spots at these three locations. These initial experiments were performed with the beam slit fully open to accept all energy particles. By virtue of its beam transport and aperture design, the transport line also does energy selection of particles, which restricts the transport up to undulator entry to a relative energy spread of $\leq$2.5%.

Further experiments on the commissioning of the transport line were performed with a 5 $\mu$s macropulse width of the electron beam with 0.8 nC charge per micropulse from the electron gun. Experiments were performed to study energy selection of particles within the required 0.5–0.75% relative energy spread window necessary for FEL operation using the energy selection slit. The quadrupoles after the linac were adjusted to achieve a small horizontal beam size with high dispersion at the beam slit location after the first bend to be able to select a high-energy beam with RMS energy spread of 0.45% or more as per requirement. A slit opening of 3.7 mm corresponds to an energy spread selection of 1%.

From figure 3, it can be seen that the profile of the measured ICT trace is reasonably flat and it is not affected by the variation of RF phases in the pre-buncher or linac because charge with all mean energies and relative energy spread is transmitted through the injector system with minimum loss. However, the amplitude and profile of the energy-selected beam measured at ICTs 4–6 depends very critically on the phase settings in the pre-buncher and linac structures for a given setting of the transport line and the energy selection slit. The flatness of the ICT profiles at these locations is poor due to the poor stability of RF amplitude and phase over a macropulse. The magnitude of charge in

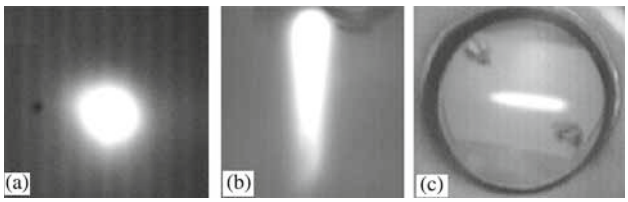


**Figure 5.** Beam profile (**a**) at the linac exit, (**b**) near the energy selection slit and (**c**) at the undulator entrance.

the energy-selected electron beam (ICT4–6) shows an almost three-fold increase with the pre-buncher set at optimum phase and power with respect to the phase in the two linac structures. For example, the magnitude of the peak energy-selected charge could be increased from $\sim$0.1 to $\sim$0.3 nC in an experiment with the pre-buncher phase set at an optimum value, and the relative phase difference between the two PWT linac structures is optimised to obtain highest transmission of the energy-selected beam. This is in line with the four-fold increase in energy-selected beam current predicted by simulations of the injector system when the pre-buncher phase and power are optimised. For the non-energy selected beam, there is not much difference in transmission through the linac with or without the pre-buncher, as also predicted by beam dynamics simulations. The spent beam coming out from the IR-FEL optical cavity has a larger energy spread compared to the input beam at undulator entry, and the transport line section from the undulator exit to the beam dump has been designed with large physical aperture for lossless transport of this electron beam up to the dump. The charge calculations show that there is no loss of electron beam during its transport through the undulator, which is desirable to minimise the harmful effect of radiation on the undulator magnets. Practically, however, a very small fraction of electron beam may be lost, which is detectable by the Bolometer. Fine tuning of the transport line magnets is done by minimising the Bolometer signal corresponding to the Bremsstrahlung radiation background due to beam loss.

## 5. Characterisation of the electron beam

The accelerated electron beam in the IR-FEL set-up has been characterised by measuring its transverse size, charge per micropulse, emittance, mean energy and relative energy spread. The transverse size of electron beam is measured at different locations along the beam transport line using the triggered GigE CCD cameras [3] and an image acquisition and analysis software developed in-house. The BPMs used for beam viewing use chromax screens which saturate with high charge dumped on the screen. The CCD cameras also saturate

with very high fluorescence from the chromax screens in experiments with high charge per macropulse. To get over the problem of saturation of the screens and the camera, very short macropulses of ∼0.1–0.2 $\mu$s are used with low charge per micropulse (<0.1 nC) in the electron beam. For a micropulse spacing of ∼33.6 ns (29.75 MHz), it translates to around 3–6 microbunches in each macropulse of ∼0.1–0.2 $\mu$s. The saturation of the CCD cameras is avoided by using neutral density (ND) filters with appropriate attenuation to acquire a clean Gaussian beam profile using the image acquisition and analysis software. Before commissioning the image analysis software, beam sizes were measured at different locations along the beam line by triggered acquisition and offline analysis of the image after calibrating the pixel size. Figure 6a shows the captured beam spots at the straight end for a round beam with two different ND filters, and figure 6b shows the corresponding beam profile with a Gaussian fit. These figures clearly show that the effect of saturation has been eliminated by employing ND filters. The RMS beam sizes measured in this experiment are 0.9 and 1.0 mm for the two different fittings corresponding to two different ND filters for the same beam spot, considering calibration as 1 pixel = 65 $\mu$m. Figure 7 shows the transverse electron beam profile at the undulator exit, obtained using the image acquisition and analysis software. The measured beam sizes are $\sigma_x = 2.4$ mm and $\sigma_y = 1.25$ mm. The peak charge per micropulse is measured using an ICT as discussed earlier.

The emittance of the accelerated electron beam is measured by employing the quadrupole scan technique. The quadrupole scan technique is the most widely used method for measuring the transverse emittance in the accelerator. In this technique, the transverse size of the beam measured at an imaging station (typically at a BPM location) is a function of the magnetic field strength of a quadrupole magnet, which is varied to find the minimum spot size at the imaging station. By plotting the square of the beam size as a function of the quadrupole strength and applying a parabolic fit, one gets the coefficients required to calculate the transverse emittance of the beam. During the experiments, the quadrupole QP4F and the imaging station BPM 13 are used, which are marked in figure 1 showing a schematic of the IR-FEL lay-out. A very short macropulse of <0.1 $\mu$s was used in these experiments, to avoid saturation of the screens due to high pulse charge. The variation of the square of RMS beam size in horizontal plane as a function of the quadrupole field strength is shown in figure 8. The Twiss parameters of the electron beam at the entry to QP4F have been measured to be $\beta_x = 7$ m and $\alpha_x = -17$. The experiments have been repeated for different operating conditions of the electron gun and

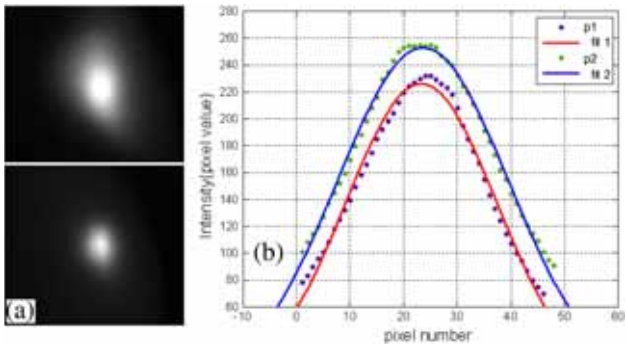


**Figure 6.** (**a**) Captured electron beam spots for two different ND filters and (**b**) beam profile for the two acquired spots with Gaussian fit.

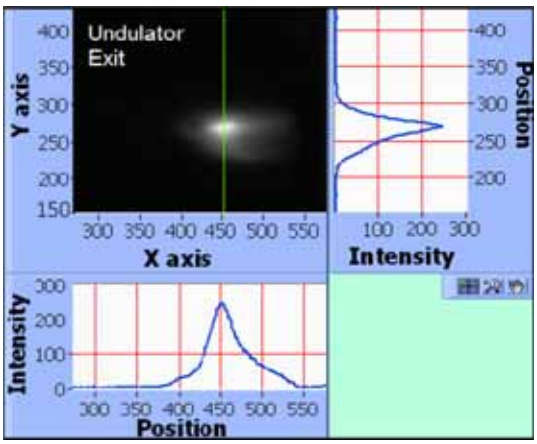


**Figure 7.** Transverse electron beam profile at the undulator exit obtained using the image acquisition and analysis software.

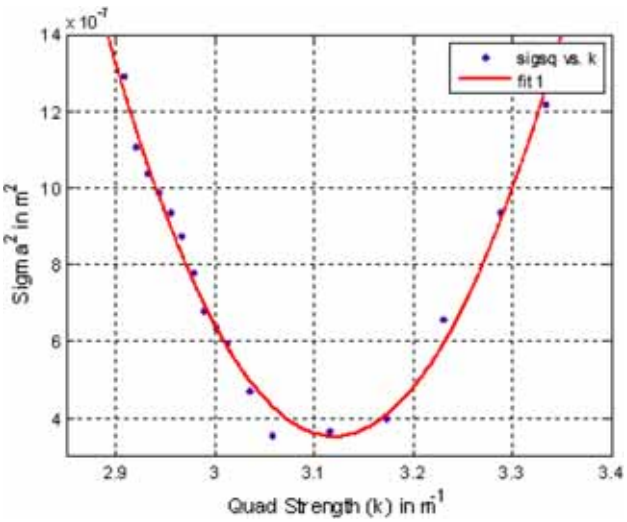


**Figure 8.** Plot of the experimental values of the square of RMS size vs. quad strength with second degree polynomial fit.

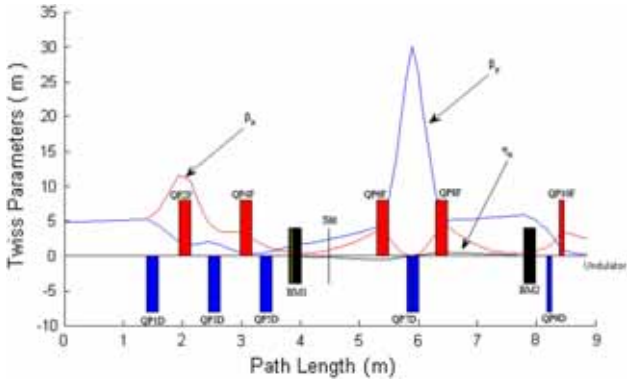


**Figure 9.** The design lattice of the IR-FEL beam transport line from the linac exit to the undulator entrance.

the Twiss parameters at the exit of the linac have been determined to be $\beta_x = 8.7$ m, $\beta_y = 18.1$ m, $\alpha_x = 9.4$ and $\alpha_y = 4.68$. The measured RMS normalised emittance using this technique was ∼44 mm mrad.

The optics design of the IR-FEL electron beam transport line, from the linac exit to the undulator entrance point, was carried out to match the transverse phase space parameters (i.e. Twiss parameters) of the beam at the undulator entrance point in such a way that minimum loss of particles takes place during the transport process. As per the design requirement of the IR-FEL system, the beam transport line has a dog-leg-type achromatic lattice. TRANSPORT code has been used to design this line. Figure 9 shows the design of the beam transport line from linac exit point to undulator entrance point. From the simulations, the normalised emittance is 30 mm mrad and the Twiss parameters at the linac exit are $\beta_x = 4.9$ m, $\beta_y = 4.9$ m, $\alpha_x = 0$ and $\alpha_y = 0$. In the IR-FEL electron beam transport line, the mean energy of the electron beam transported to the undulator entry is chosen by setting the bending magnets at the desired field strength, while a fixed relative energy spread window is selected by fixing the width of the energy selecting slit. When a macropulse having several electron microbunches propagates through this arrangement, a jitter in the mean energy over a macropulse or a variation in relative energy spread in each micropulse is manifested by a variation in the peak energy-selected charge transported over the macropulse up to the undulator entry.

This variation over a macropulse is illustrated by figures 10a–10d, which show the variation of charge over an accelerated macropulse for the same operation parameters of the injector system and the electron beam transport line, but with different settings of the energy selecting slit. It is clear that the uniformity of the accelerated electron beam over a macropulse becomes poorer as the slit is set to smaller energy

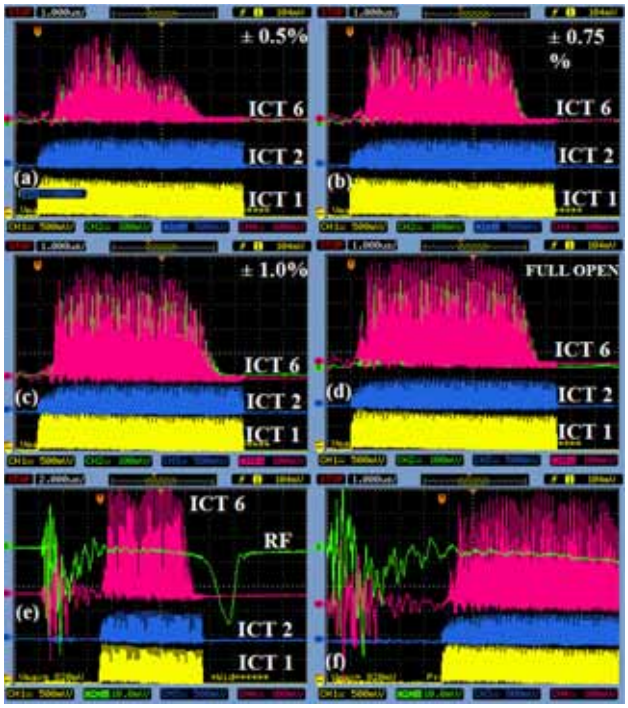


**Figure 10.** ICT6 traces of the accelerated electron beam at the undulator exit for different settings of the energy selecting slit. Traces (**a**)–(**d**) show the ICT6 traces for energy selecting slit set to accept 0.5, 0.75, 1.0% and full beam. Trace (**e**) shows the position of the electron beam (ICT6) over the flattest portion of the RF macropulse (green) and trace (**f**) shows a zoomed version of the same.

spread setting. The opening of the slit does not affect the RF pulse profile, but it affects the profile of the energy-selected electron macropulse. An ideal flat profile of the energy-selected electron beam macropulse is expected if the RF macropulse also has a flat amplitude profile and good phase stability over a macropulse. However, any deviation in the RF amplitude and phase stability over a macropulse results in the accelerated electron beam macropulse having different mean energy and also different relative energy spread over different portions of the macropulse. When this accelerated electron beam macropulse is put through an energy-selecting slit, portions where the mean energy and relative energy spread matches the setting of the slit and the transport line parameters have the highest charge (highest ICT voltage signal) and portions with poorest matching has the lowest charge (lowest ICT voltage signal). Therefore, the profile of the energy-selected electron beam macropulse is not flat but has large amplitude variation. If the slit is opened fully, then there is no energy selection and all the charge with different mean energies and different relative energy spread is transported by the HEBT. Hence, the profile of the energy-selected electron beam macropulse is smooth and flat. As the energy-selected slit is closed to select 1% relative energy spread

particles, the effect of variation in RF amplitude and phase over a macropulse becomes apparent in the profile of the accelerated electron beam macropulse in the form of non-uniformity in ICT signal over a macropulse. For a smaller relative energy spread selection, the variation is more significant because the fraction of charge within the selected relative energy spread becomes smaller. Hence, the profile shows more variation. As per simulations, the IR-FEL requires a flat energy-selected beam with a peak current of 30 A over a macropulse duration greater than 3 $\mu$s for lasing. The power output from the IR-FEL will vary over this initial 3 $\mu$s period till the FEL saturates. Hence, it is good to have a larger electron beam macropulse (>5 $\mu$s) such that the user gets some duration of constant IR power output for experiments after saturation of the FEL.

In order to further analyse the effect of quality of RF flat-top on the variation in the energy-selected charge per micropulse over a macropulse, a novel method is adopted which involves the acceleration of short electron macropulses (400 ns) with different injection times in the RF macropulse, and its subsequent analysis at the undulator entry after energy selection. In this experiment, the operating parameters of the injector system are kept constant and the energy selection slit width is also kept constant. Ideally, after an initial time period corresponding to approximately three fill times of RF in the linac structures (~2 $\mu$s), the accelerating electric field should achieve a constant amplitude for the remaining portion of the RF macropulse. If the phase is also stable over the macropulse, then a short electron bunch injected over any portion of the RF pulse after the initial fill time should be accelerated to the same mean energy with the same relative energy spread. If the gun delivers uniform charge over a macropulse, then the accelerated electron macropulse should have a flat profile after the energy selection, which means that the ICT trace for the energy-selected electron beam at the undulator entry should show a constant amplitude for different injection times of the short electron macropulses in the long RF macropulse. In our experiment, it is observed that the amplitude of the ICT signal varies significantly as the electron pulses are injected at different times on the RF macropulse, which could be due to significant variation in amplitude and phase of the RF over a macropulse, and pulse-to-pulse variation in the RF because the energy-selected beam pulse is monitored over different electron beam macropulses. Figure 11a shows the reference position of a short (400 ns) electron macropulse in the RF macropulse (red), while figures 11b–11h show the ICT traces of the energy-selected electron bunches (green) injected with different time delays with respect to the reference position in figure 11a. The quality of flat top and phase stability of RF over a macropulse will

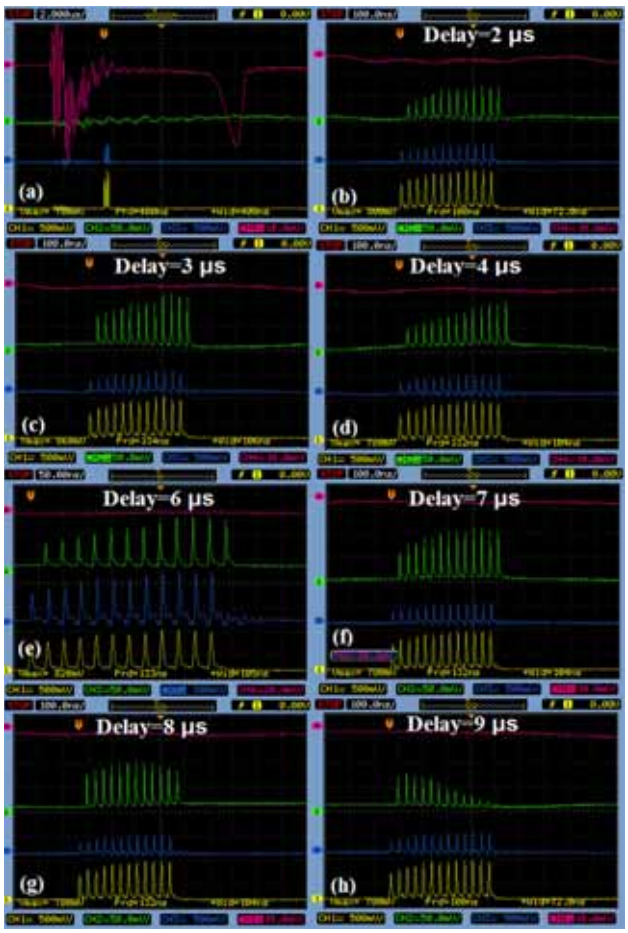


**Figure 11.** ICT traces of energy-selected short bunch (400 ns) electron beam injected into the RF macropulse with different time delays. Trace (**a**) reference position of the electron bunch and traces (**b**)–(**h**) with different time delays with respect to the reference time.

determine the accelerating field amplitude and phase seen by the short electron bunch in each of these time-delay positions. In order to eliminate the role of the pre-buncher RF in these experiments, the electron beam from the gun was injected directly into the PWT linac structure without powering the pre-buncher. The traces were recorded after the optimisation of the phase of S-band RF in the two PWT linac structures for best transmission of energy-selected pulse. Since a short electron bunch is extracted from the gun in these experiments, the ICT trace of the electron beam from the gun (yellow) in all the cases shows an initial rise time for the electron beam from the gun after which it attains the same amplitude in all cases. The maximum amplitude of the energy-analysed (green) signal in figures 11b–11h, however, shows a very significant variation from ~70 to 110 mV. The energy selection in these experiments was set at 1%, and a more significant variation has been observed in experiments when a smaller energy spread

**Table 3.** Comparison of design and measured parameters of IR-FEL.

| Parameters | Design values | Measured values |
|---|---|---|
| Emittance (mm mrad) | 30 | 44 |
| Energy spread (%) | 0.5 | 0.75 |
| Peak current (A) | >30 | 26 |
| Macropulse width ($\mu$s) | 8 | 4.5 |
| Repetition rate (Hz) | 10 | 1 |
| Enhancement over spontaneous power | $10^7$ times | $10^5$ times |

**Table 4.** Measured beam parameters during lasing.

| | |
|---|---|
| Radiation wavelength | 35 $\mu$m |
| Electron beam energy | 18.4 MeV |
| RMS normalised emittance | 44 mm mrad |
| Peak current | 26 A |
| Macropulse width | 4.5 $\mu$s |
| Relative energy spread | 0.75% |
| Undulator period ($\lambda_u$)/length | 50 mm/2.5 m |
| RMS undulator parameter ($K$) | 0.916 |
| Undulator gap | 32 mm |
| Optical cavity length | 5.038529 m |
| Out coupling hole radius | 1.75 mm |

selection is chosen using the slit. The results from this experiment show good qualitative agreement with the observation of variation of energy-selected beam charge over a macropulse as shown in figures 10a–10d. Table 3 compares the designed vs. measured values of electron beam and RF parameters.

## 6. IR-FEL simulations for the measured electron beam parameters

The first observed signature of lasing in IR-FEL has resulted in a power output that is $\sim 10^5$ times the expected spontaneous emission power as reported in ref. [13]. The estimated out-coupled peak micropulse power during these experiments is ~2 kW at a wavelength of 35 $\mu$m with an electron beam energy of 18.4 MeV. The measured electron beam parameters during the experiment are given in table 4.

We have performed time-dependent oscillator simulations using the code GINGER [13] after considering the measured electron beam parameters, in order to verify with the experimental results. A Gaussian electron beam profile was considered with an RMS width of 4 ps and a peak current of 24 A. As the measured electron beam profile considered at the undulator entrance shows a variation in the charge in each micropulse over a macropulse in the energy-selected beam, the simulations considered a mean value of 24 A as the peak current in each micropulse instead of the measured peak current of 26 A at the undulator entry. In the GINGER code, the total number of radiation slices should be a power of two in order for the fast-Fourier transform (FFT) spectral decomposition in the post-processor to run properly [13]. We have chosen the total number of radiation slices as 256, with the spacing between slices taken as one radiation wavelength. Out of this, 205 electron slices were used to cover six times the electron RMS bunch length, and the remaining slices correspond to the slippage length, i.e. $N_u$ (number of undulator periods) times the radiation wavelength. For the optimum performance of the FEL, the actual cavity length has to be detuned slightly from the synchronous cavity length. At optimum cavity length, the overlap will be best between the electron beam and the optical beam and the out-coupled power will be maximum. The optimum cavity detuning found from simulations was 26 $\mu$m, which agrees well with the observed detuning length of 21 $\mu$m during the actual experiments. Figure 12a shows the growth of intracavity IR power as a function of pass number. Here we assumed a long macropulse of ~15 $\mu$s to show the saturation. The power level during the first lasing is marked in the same plot (macropulse width during the experiments is ~5 $\mu$s), and it is much below saturation. Figure 12b shows the time structure of the optical pulse at saturation and figure 12c shows the power spectrum at saturation. The estimated small signal gain using an analytical formula is 29% and the round trip cavity loss for this cavity is 15%. The net single pass gain thus comes to 9.7%. The net gain as calculated from GINGER is 10%, which is in good agreement with analytical results. The expected spontaneous power for the experimental parameters is 165 $\mu$W. The average intracavity power in 5 $\mu$s predicted by simulations is 5.36 W which is an enhancement by $\sim 3.2 \times 10^4$ times over the expected spontaneous power for beam parameters used in the experiment. The predicted enhancement factor agrees reasonably with the experimentally estimated value of $\sim 7 \times 10^4$. The estimated peak out-coupled power of 2 kW (in 10 ps) during the experiments agrees reasonably with 2.7 kW, the value predicted by the simulations.

## 7. Conclusion

The successful commissioning of the injector and electron beam transport systems of the IR-FEL has led to the first lasing in the set-up, where a power gain of $\sim 10^5$ over expected spontaneous radiation power has been reported [1]. The FEL design simulations predict a gain of $10^7$ with an output peak power of 2 MW and

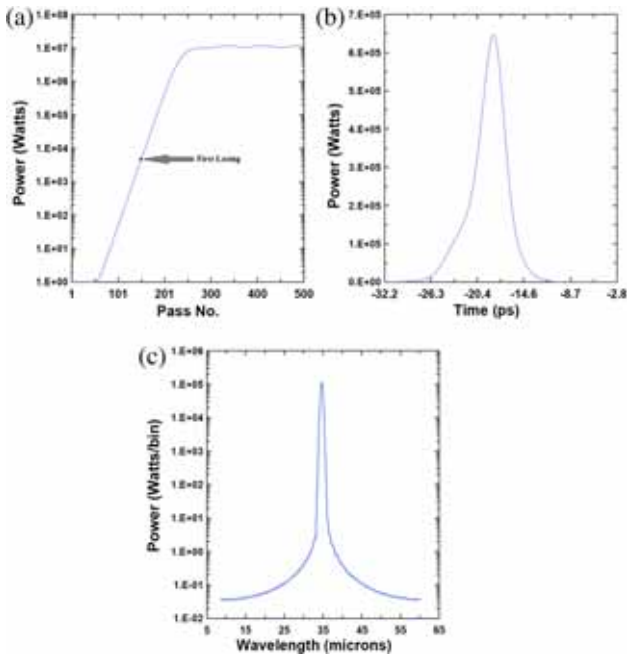


**Figure 12.** (**a**) Growth of average intracavity power as a function of pass number (averaging is done over 10 ps), (**b**) time structure of the out-coupled radiation at saturation and (**c**) power spectrum at saturation as per GINGER.

a CW average power of 30 mW at 10 Hz operation, with a beam peak current more than 30 A and timing jitter of the order of 1–2 ps. While the measured peak current of 26 A in these experiments is lower than the required value of >30 A as per FEL simulations, the measured 35–45 mm mrad emittance of the accelerated electron beam is acceptable as indicated by FEL simulations. The measured electron beam macropulse width with the best observed flatness of the energy-analysed charge over the macropulse is ∼4.5 $\mu$s for an energy spread window of 0.75%. Here again, there is a significant variation in the charge per micropulse over the macropulse width resulting in net average energy analysed charge being lower than the peak measured value of 0.26 nC. FEL simulations performed for these operational electron beam parameters also indicate a gain that is lower by 2–3 orders of magnitude than the expected power gain for the design electron beam parameters for the IR-FEL.

The injector system is presently in the process of being upgraded to achieve a significant increase in the peak current at the undulator entry from the present value of 25–30 to ∼50 A, with a good uniformity of the energy-selected beam over each macropulse. During the first lasing, the peak current was ∼26 A, with a macropulse width of ∼5 $\mu$s, corresponding to 148 passes. Figure 12a shows that the power level achieved during the first lasing is much below saturation. For saturation, at least 250 passes are required corresponding to a 7.5 $\mu$s long macropulse with good uniformity. After the injector system upgrade, which aims to increase the peak current to ∼50 A, FEL simulations predict saturation in just 100 passes (macropulse width ∼3.5 $\mu$s), with a significantly higher power output from the IR-FEL.

## Acknowledgements

The FEL development was done under a collaborative effort of different divisions of RRCAT in areas of RF and microwaves, vacuum, magnets, power supplies, alignment, workshops and controls. Their very valuable contribution is greatly acknowledged. Technical assistance of Mr Rajkumar Bhowate is also greatly acknowledged.

## References

[1] K K Pant *et al*, *Curr. Sci.* **114**, 2 (2018)
[2] S Chandran, B Biswas, S Lal, A Kumar, R K Pandit, P Nerpagar, S K Gupta, A K Sarkar, M Khursheed and K K Pant, *Proceedings of InPAC* (RRCAT, Indore, 2018) ID 273, pp. 1-3
[3] V Kumar, B Biswas, U Kale, A Kumar, Shankar Lal and K K Pant, *Proceedings of InPAC* (IUAC, New Delhi, 2011) ID 108, pp. 1–2
[4] A Kumar, *Proceedings of InPAC* (RRCAT, Indore, 2009) ID 109, pp. 1–3
[5] R S Saini, B Biswas, K K Pant, A D Ghodke and G Singh, *Proceedings of InPAC* (IUAC, New Delhi, 2011) ID 217, pp. 1–2
[6] S Chouksey, S Lal, S K Gupta, A Kumar, B Biswas, S S Parihar, K K Pant and S Krishnagopal, *Proceedings of InPAC* (IUAC, New Delhi, 2011) ID 223, pp. 1–2
[7] S Chouksey, S Krishnagopal, V Kumar, S Lal and K K Pant, *Proceedings of APAC* (Indore, 2007) pp. 479–481
[8] S Lal and K K Pant, *Rev. Sci. Instrum.* **87**, 083308 (2016)
[9] S Chandran and B Biswas, *Nucl. Instrum. Methods Phys. Res. A* **798**, 121 (2015)
[10] S Lal, K K Pant and S Krishnagopal, *Proceedings of IPAC'10* (Kyoto, Japan, 2010) pp. 1713–1715
[11] S K Gupta, Shankar Lal, R K Pandit and K K Pant, *Proceedings of InPAC* (RRCAT, Indore, 2018) ID 08, pp. 1–3
[12] B Biswas, U Kale, M Khursheed, A Kumar, V Kumar, Shankar Lal, P Nerpagar, A Patel and K K Pant, *Curr. Sci.* **105**, 1 (2013)
[13] W Fawley, *A user manual for GINGER and its post-processor XPLOTGIN LBNL-49625-Rev*, Ist edn (Lawrence Berkeley National Laboratory, Berkeley, 1997)